



Structural control on earthquake behaviors revealed by high-resolution V_p/V_s imaging along the Gofar transform fault, East Pacific Rise

Hao Guo ^a, Haijiang Zhang ^{a,*}, Berenice Froment ^b

^a Laboratory of Seismology and Physics of Earth's Interior, School of Earth and Space Sciences, University of Science and Technology of China, Hefei, Anhui, China

^b Institut de Radioprotection et de Sûreté Nucléaire (IRSN), Fontenay-aux-Roses, France

ARTICLE INFO

Article history:

Received 12 February 2018

Received in revised form 23 July 2018

Accepted 24 July 2018

Available online xxxx

Editor: M. Ishii

Keywords:

oceanic transform fault

temporal and spatial earthquake evolution

fault segmentation

double-difference tomography

V_p/V_s inversion

ABSTRACT

The Gofar transform fault (GTF), 4°S on the East Pacific Rise, can generate M_w 5.5–6 earthquakes quasiperiodically on some specific patches that are separated by stationary rupture barriers. Small earthquakes along strike show a clear spatial and temporal evolution. To better understand the cause of the observed behaviors of large and small earthquakes, we have determined high-resolution earthquake locations within a period of one year covering the 2008 M_w 6.0 (M6) earthquake, as well as V_p , V_s , and V_p/V_s models along the westernmost segment of the GTF, using a well recorded ocean bottom seismograph dataset and a new V_p/V_s model consistency-constrained double-difference tomography method. Compared to the previous P-wave tomography study in this area, the use of a new automatic arrival picking algorithm significantly improves the accuracy of S-wave arrival times, thereby allowing for the inversion of V_s and V_p/V_s models in addition to V_p model. High-precision waveform cross-correlation differential times are also used. The tomographic V_p/V_s model reveals strong structural variations at multiple scales along the fault, which likely control the behaviors of large and small earthquakes. The M6 mainshock is generated within a specific ~8-km-long fault patch composed of intact rocks. By contrast, multiple fluid-filled damaged zones on both sides of this asperity are imaged and have varying size which is suggested to be critical in their ability of stopping ~M6 ruptures. High-resolution earthquake relocations and velocity models also indicate that the occurrence of small earthquakes is also correlated with structural variations. Combined with previous studies, our results further suggest that strong structural variations control the fault mechanics and earthquake behavior along the GTF.

© 2018 Elsevier B.V. All rights reserved.

1. Introduction

Faults can slip in different modes, including slow slip, non-volcanic tremor, steady creep, microseismicity, and large dangerous earthquakes (Ide et al., 2007; Peng and Gomberg, 2010), but our understanding of their physical mechanisms is still very limited (Harris, 2017). In contrast to continental faults, mid-ocean ridge transform faults (RTFs) provide a better tectonic environment for studying how fault zone physical properties influence fault slip and earthquake behaviors because they have relatively simple geometries with average slip rates that are well defined by plate spreading velocities, and show, in general, more homogeneous compositions and more predictable thermal structures (Boettcher and Jordan, 2004; Roland et al., 2012).

The Gofar transform fault (GTF), located 4°S on the East Pacific Rise (EPR), has three fault segments (G1, G2, and G3) separated by intratransform spreading centers (Fig. 1a) and can generate M_w ~6 (M6) earthquakes quasiperiodically every 5 to 6 years on some specific fault patches (McGuire, 2008). In this study, we focus on the short (~90 km) and high-slip-rate (~14 cm/yr) westernmost segment (G3) of the GTF (Fig. 1a). The G3 has two distinct asperity patches (red and orange ellipses in Fig. 1b) that repeatedly generate M6 earthquakes and are separated by a stationary rupture barrier patch that can stop the propagation of M6 earthquakes (Fig. 1b) (McGuire et al., 2012).

In 2008, motivated by the observed regular EPR seismic cycles (McGuire, 2008), Woods Hole Oceanographic Institution (WHOI) deployed 16 ocean bottom seismographs (OBS) around the G3 fault segment for one year of continuous monitoring. This experiment successfully captured a M6 earthquake that occurred on 18 September 2008 on G3 (red star in Fig. 1b) (McGuire et al., 2012). In addition, a wide-angle seismic refraction survey line was also

* Corresponding author.

E-mail addresses: hguo@mail.ustc.edu.cn (H. Guo), zhang11@ustc.edu.cn (H. Zhang), berenice.froment@irsn.fr (B. Froment).

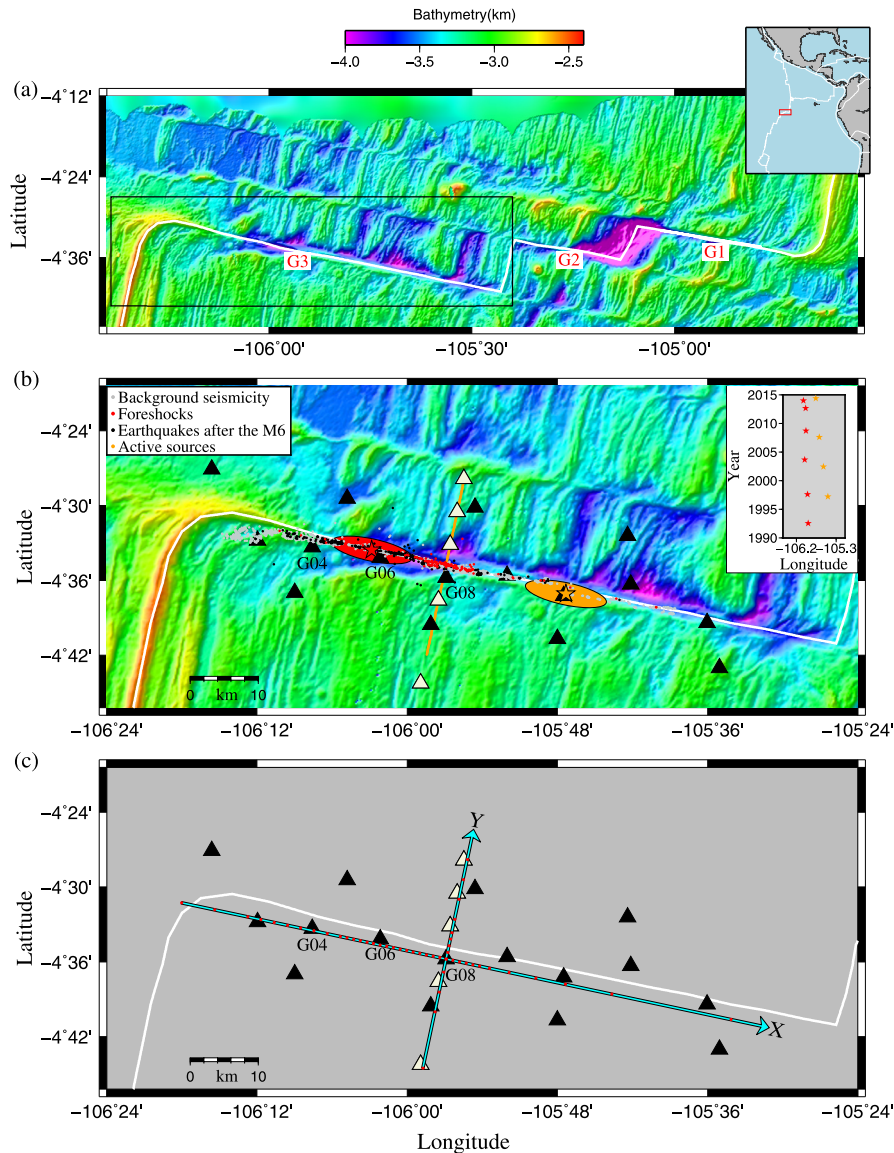


Fig. 1. (a) Gofar transform fault system, including three fault segments (G1, G2, and G3) separated by intratransform spreading centers. The black rectangle outlines the G3 segment shown in Fig. 1b. White line shows the plate boundary. The inset map in the upper-right corner shows the geographic location of the GTF. (b) Distribution of earthquakes and stations around G3. Black triangles represent the OBS sites deployed for the one-year passive-source experiment in 2008, among which stations G04, G06 and G08 are labeled. Beige triangles represent the OBS sites deployed for the active-source experiment. Orange dots forming a line represent the active-source air-gun shots across the fault. Grey, red, and black dots represent the relocations of background earthquakes, foreshocks, and the earthquakes after the mainshock with small location uncertainties, respectively. Note that compared to Fig. 6a, here the relocations after the mainshock are within 20 days after the mainshock. Red and orange ellipses represent ~10-km-long asperity patches centered on the centroid locations of the 2008 M_w 6.0 (red star) and 2007 M_w 6.2 (orange star) mainshocks, respectively. The centroid locations of these two M6 mainshocks were determined by McGuire et al. (2012). As shown in the temporal evolution plot in the upper-right, these two patches generate large earthquakes (i.e. red and orange stars in the upper-right plot) every ~5–6 years (note that the locations of these large earthquakes are from GCMT catalog, which has relatively large location uncertainties. See McGuire (2008) for details on how the overlapping rupture patches of these large earthquakes are defined). (c) Horizontal Cartesian coordinate system and grid setting for the inversion. The X and Y axes of the Cartesian coordinate system are represented by cyan lines, with arrows pointing to the positive directions. The coordinate center is located at G08. The Y axis is rotated 12° clockwise from North so that the X axis is parallel to the fault strike. The grid nodes (red dots) on the coordinate axis are positioned at $X = -40, -35, -30, -28, -26, -24, -22, -20, -18, -16, -15, -14, -13, -12, -11, -10, -9, -8, -7, -6, -5, -4, -3, -2, -1, 0, 1, 2, 3, 4, 5, 6.5, 9.5, 13.5, 18, 25, 43$ km, and $Y = -16.5, -8, -5, -2, 0, 1, 2, 3, 4, 6, 9, 12, 15$ km. Note that the G3 active fault trace is at about $Y = 2$ km. (For interpretation of the colors in the figure(s), the reader is referred to the web version of this article.)

conducted across the rupture barrier patch (Fig. 1b) (Roland et al., 2012).

Using the 2008 1-year-long OBS array dataset, McGuire et al. (2012) detected and located tens of thousands of earthquakes, including a 1-week-long sequence of foreshocks preceding the 2008 M6 mainshock, aftershocks, an earthquake swarm that occurred in December, as well as the background seismicity that occurred before foreshocks (Fig. 1b). This 1-year-long seismicity showed along-strike variations in earthquake rupture properties. McGuire et al. (2012) suggested that the ~10-km rupture barrier patch (defined as Patch 1 in this paper), associated with abundant foreshocks and

deep seismicity, could stop the mainshock rupture, probably as a result of enhanced fluid circulation.

Using the active-source seismic dataset, Roland et al. (2012) determined a 2-D P-wave tomography model across the fault, which just passed through the rupture barrier patch (Fig. 1). A low-velocity fault zone throughout the crust was imaged and interpreted to be highly damaged with enhanced fluid-filled porosity (Roland et al., 2012).

Combining both datasets, Froment et al. (2014) complemented the work of Roland et al. (2012) by determining the along-strike V_p model using the double-difference (DD) tomography method

(Zhang and Thurber, 2003). Froment et al. (2014) found higher V_p in the 2008 M6 rupture patch (Patch 2, defined later) at seismogenic depths than in its adjacent fault patches and suggested that the mainshock rupture patch was composed of relatively intact rock while rocks of its adjacent fault patches were damaged. Moreover, the use of DD tomography method in Froment et al. (2014) improved the earthquake locations of McGuire et al. (2012) that were determined with a fixed 1-D velocity model.

In Froment et al. (2014), however, only the V_p model along strike was inverted and the V_s model was not determined because of the poor quality of the S-wave arrival picks (see Section 2.2). It is known that V_s , and especially V_p/V_s , are more sensitive than V_p to the existence of fractures and fluids (Kuster and Toksöz, 1974; Takei, 2002). In this study, we jointly invert earthquake locations, V_p , V_s , and V_p/V_s models along the G3 segment of the GTF, using an improved earthquake dataset and an improved tomography method. New results are able to characterize high-resolution fault-zone structures, which can help us to better understand the relationship between structural variations and various earthquake behaviors along the fault.

2. Method and dataset

2.1. V_p/V_s model consistency-constrained DD tomography method

In this section, we first introduce the original DD tomography method (Zhang and Thurber, 2003; Zhang et al., 2009) that jointly inverts earthquake locations, V_p , V_s , and V_p/V_s models. Then, we introduce a new V_p/V_s model consistency constraint, which can be used to determine better V_p/V_s model.

The P- or S-wave arrival time residual r_k^i between the observed $(T_k^i)^{obs}$ and calculated $(T_k^i)^{cal}$ arrival times from event i to station k , can be linearly related to the perturbations of earthquake location in three directions (dx_1, dx_2, dx_3), earthquake origin time ($d\tau$), and slowness (δu) along ray path elements (ds), as follows,

$$r_k^i = (T_k^i)^{obs} - (T_k^i)^{cal} = \sum_{m=1}^3 \frac{\partial T_k^i}{\partial x_m^i} dx_m^i + d\tau^i + \int_i^k \delta u ds \quad (1)$$

Following Thurber (1993), by assuming identical P- and S-wave ray paths, the S-P arrival time residual (r_{ksp}^i) between the observed $(T_{ksp}^i)^{obs}$ and calculated S-P arrival times $(T_{ksp}^i)^{cal}$ from event i to station k can be linearly related to the perturbations of earthquake location and the ratio of V_p to V_s ($\delta(V_p/V_s)$) along the ray path, as follows,

$$\begin{aligned} r_{ksp}^i &= (T_{ksp}^i)^{obs} - (T_{ksp}^i)^{cal} \\ &= \sum_{m=1}^3 \left(\frac{\partial T_{ksp}^i}{\partial x_m^i} - \frac{\partial T_{kp}^i}{\partial x_m^i} \right) dx_m^i + \int_i^k \frac{\delta(V_p/V_s)}{V_p} ds \end{aligned} \quad (2)$$

The event origin time term can be canceled out using S-P times. It is also noted that the OBS clock errors (Gouédard et al., 2014) can be removed using S-P times because the clock errors of P- and S-wave arrival times for common earthquakes on common stations are the same.

By subtracting a similar equation for a nearby event j recorded at station k from equation (1), we obtain the so-called double difference dr_k^{ij} (i.e. the residual between the observed and calculated event-pair differential times) to solve for the perturbations of earthquake locations and slowness models, as follows,

$$dr_k^{ij} = (T_k^i - T_k^j)^{obs} - (T_k^i - T_k^j)^{cal}$$

$$\begin{aligned} &= \sum_{m=1}^3 \frac{\partial T_k^i}{\partial x_m^i} dx_m^i + d\tau^i - \sum_{m=1}^3 \frac{\partial T_k^j}{\partial x_m^j} dx_m^j - d\tau^j \\ &\quad + \int_i^k \delta u ds - \int_j^k \delta u ds \end{aligned} \quad (3)$$

Similarly, by subtracting a similar equation for a nearby event j recorded at station k from equation (2), we obtain the residual dr_{ksp}^{ij} between the observed and calculated event-pair differential S-P times to solve the perturbations of earthquake locations and V_p/V_s model, as follows,

$$\begin{aligned} dr_{ksp}^{ij} &= (T_{ksp}^i - T_{ksp}^j)^{obs} - (T_{ksp}^i - T_{ksp}^j)^{cal} \\ &= \sum_{m=1}^3 \left(\frac{\partial T_{ksp}^i}{\partial x_m^i} - \frac{\partial T_{kp}^i}{\partial x_m^i} \right) dx_m^i - \sum_{m=1}^3 \left(\frac{\partial T_{ksp}^j}{\partial x_m^j} - \frac{\partial T_{kp}^j}{\partial x_m^j} \right) dx_m^j \\ &\quad + \int_i^k \frac{\delta(V_p/V_s)}{V_p} ds - \int_j^k \frac{\delta(V_p/V_s)}{V_p} ds \end{aligned} \quad (4)$$

The original DD tomography algorithm (tomoDD, Zhang and Thurber, 2003) includes equations (1) and (3) to make use of absolute and differential arrival times. Equations (2) and (4) were further included by Zhang et al. (2009) to make use of absolute and differential P, S, and S-P times to jointly invert earthquake locations as well as V_p , V_s , and V_p/V_s models.

Due to similar ray paths outside the source region for pairs of nearby events recorded on common stations, the sensitivities of differential times (i.e. equations (3) and (4)) on V_p , V_s , and V_p/V_s model anomalies outside the source region can be largely reduced and thus the model near the source region can be better resolved. Moreover, high-precision waveform cross-correlation (WCC) event-pair differential times can be used to further improve earthquake locations and velocity models.

For the V_p/V_s inversion with the S-P data, the assumption of similar ray paths for P and S waves is critical. To solve this potential problem, P- and S-wave ray paths will be checked at each iteration to remove some S-P times from the inversion if the associated ray paths differ by more than a specified threshold (Zhang et al., 2009).

From the DD inversion with P, S, and S-P data (Zhang et al., 2009), we actually can get two V_p/V_s models. The first one is obtained by dividing the separate V_p model by the separate V_s model. This V_p/V_s model has larger uncertainty than the separate V_p and V_s models because the V_s model is generally more poorly resolved than the V_p model due to larger S-wave data errors and fewer S-wave data. The second V_p/V_s model is directly inverted from S-P data. This V_p/V_s model is more reliable but has lower resolution because the requirement of similar P- and S-wave ray paths would remove some S-P data. These two V_p/V_s models are generally not consistent either in shape or amplitude. To determine a V_p/V_s model with both high resolution and high reliability, we propose adding a consistency constraint to the two V_p/V_s models, as follows,

$$\Delta = k_1 - k_2 = \frac{u_s}{u_p} - k_2 \quad (5)$$

where $k_1 = \frac{u_s}{u_p} = \frac{V_p}{V_s}$ represents the V_p/V_s model from the division of V_p by V_s , with u_p and u_s representing the P- and S-wave slowness models, respectively. k_2 represents the V_p/V_s model inverted with S-P data. Δ is the difference between k_1 and k_2 . The misfit (denoted as $d\Delta$) between the true Δ (Δ^{true}) that is zero and the

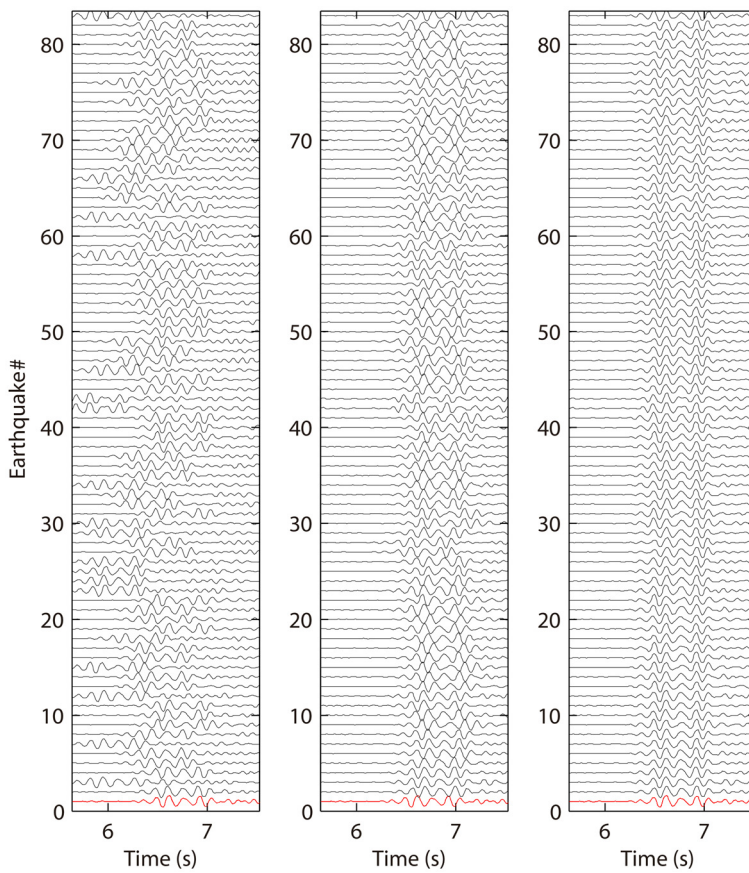


Fig. 2. Comparison of waveform alignment for 83 closely located earthquakes recorded at station G08. Black waveforms of 82 events are aligned relative to the waveform of a reference event (the red one in the bottom) based on different sets of S-wave arrival times, including (**left**) catalog arrival times, (**middle**) newly picked arrival times using the arrival picking procedure described in Section 2.2 and (**right**) arrival times converted from WCC differential arrival times. WCC converted arrival times on black waveforms are transformed from their respective WCC differential arrival times relative to the reference waveform. Waveforms are filtered between 5 and 12 Hz.

calculated one (Δ^{cal}), can be linearly related to the perturbations of u_p , u_s and k_2 (i.e. δu_p , δu_s and δk_2) by using a truncated Taylor series expansion, as follows,

$$\begin{aligned} d\Delta &= \Delta^{true} - \Delta^{cal} = k_2 - \frac{u_s}{u_p} \\ &= \frac{\partial \Delta}{\partial u_p} \delta u_p + \frac{\partial \Delta}{\partial u_s} \delta u_s + \frac{\partial \Delta}{\partial k_2} \delta k_2 \\ &= -\frac{u_s}{u_p^2} \delta u_p + \frac{1}{u_p} \delta u_s - \delta k_2 \end{aligned} \quad (6)$$

Similar to the original DD tomography method, the linear equation (6), along with (1), (2), (3), and (4), as well as the smoothing constraint, are solved by a damped least-squares algorithm (LSQR, Paige and Saunders, 1982).

By minimizing the norm of the misfit $d\Delta$, we can determine a reliable V_p/V_s model that has a similar resolution as the separate V_p and V_s models. The structure of the inverted V_p , V_s , and V_p/V_s models can also be more consistent compared to the original method of Zhang et al. (2009) without such a constraint. We test the performance of the new method in section 4.

2.2. Dataset

We start from the earthquake catalog covering the calendar year of 2008 built by McGuire et al. (2012). In this catalog, the original P- and S-wave first-arrival catalog dataset was built using the standard short-term average to long-term average ratio (STA/LTA) algorithm. In this study, we select earthquakes with at

least 14 arrivals from this original catalog. We then improve the S-wave data quality by using a new automatic arrival picking algorithm, which is based on Akaike Information Criteria (Maeda, 1985; Zhang et al., 2003) (see supplementary materials).

To demonstrate the improvement in the quality of new arrival picks, we randomly select some closely located earthquakes recorded at a common station and then align their waveforms with respect to their arrival picks (Fig. 2). Due to the similar ray-paths expected for this subset, these waveforms are expected to be highly similar around their first arrivals. After aligning these waveforms according to their original and new arrival picks, it is clear that the waveforms around new picks are much better aligned (Fig. 2), indicating the improved quality of new picks by our procedure. The comparison of traveltime-distance curves further confirms the quality improvement in new picks (Fig. S1). The root-mean-square (RMS) value of absolute differences between new and original S-wave arrival times is 0.195 s, which can be used to quantify the improvement resulting from our picking procedure.

We also use a WCC technique (Du et al., 2004) to measure differential arrival times from pairs of nearby earthquakes on common stations. The waveform alignment is further improved by using the WCC data compared to arrival picks (Fig. 2), indicating the WCC data are more accurate. In addition to the earthquake data, P-wave first arrival times from active sources recorded by 5 OBSs crossing the fault, deployed during the active-source experiment, are also included (Fig. 1b). Overall, our final dataset, listed in Table S1, includes a total of 7432 earthquakes and 271 active shots recorded by 21 OBSs.

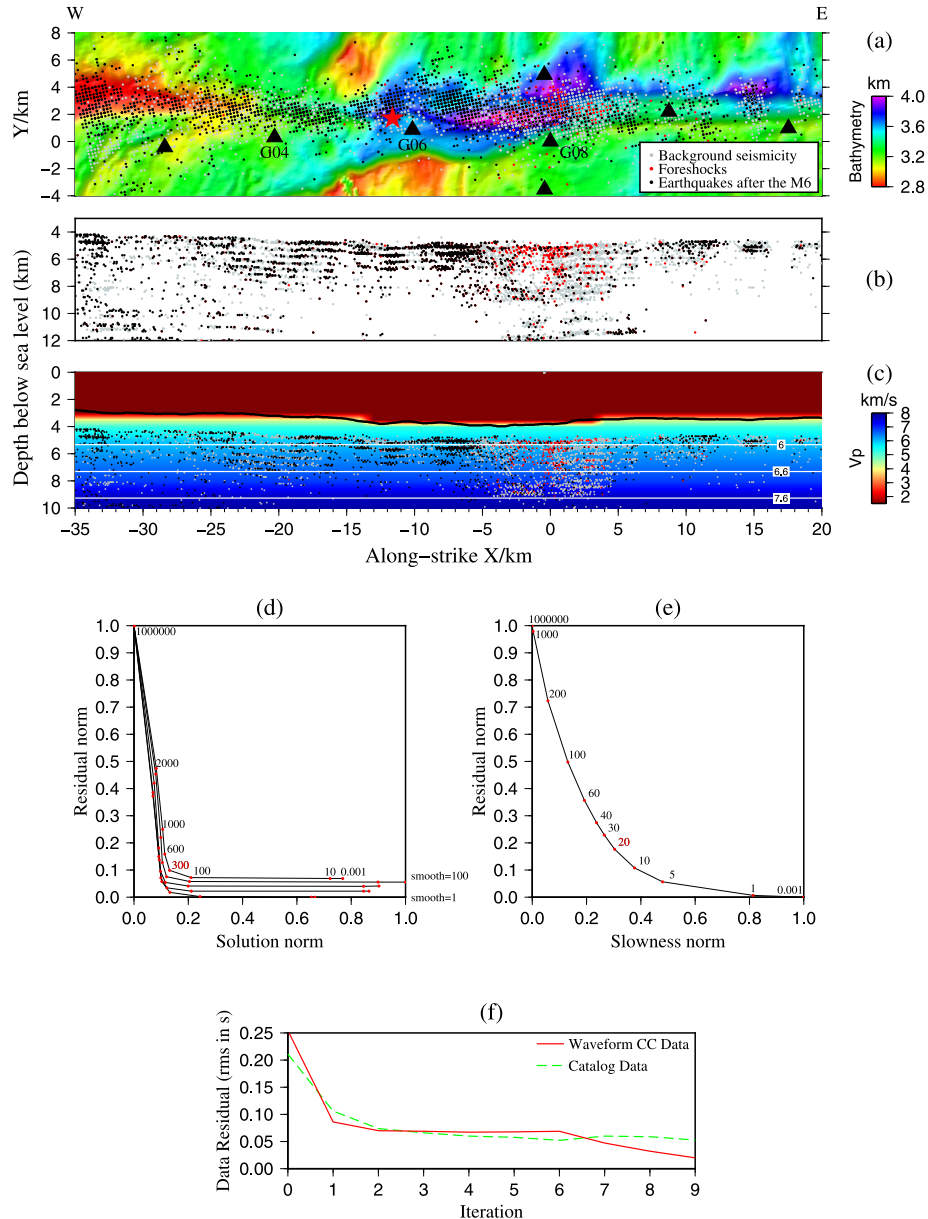


Fig. 3. Tomographic inversion details on the initial earthquake locations (a–b), the initial 1-D V_p model at the vertical cross-section of $Y = 2$ km (c), the trade-off analysis for the selection of optimal damping (d) and smoothing (e) parameters, and the evolution of the catalog and WCC data residuals with inversion iterations (f). In (c), the bold black line represents the local seafloor at $Y = 2$ km. The dark red region associated with V_p of 1.5 km/s above the sea floor represents the seawater. Note that the initial model is also adjusted to fit the topographic variation of the local seafloor. Velocity is contoured at 6.0, 6.6 and 7.6 km/s, respectively. (d) shows the trade-off analysis between the normalized solution norm and data residual norm from inversions with a set of smoothing and damping parameters. Different curves represent disparate smoothing values of 1, 10, 30, 60 and 100, with 100 at the top and 1 at the bottom. Red dots on each curve, associated with the same smoothing value, represent different damping values. Both earthquake location and slowness variables are included for the calculation of the solution norm because the damping parameter is applied to constrain the slowness and earthquake location at the same time during the joint inversion. The optimal damping parameter of 300 is selected. (e) shows the trade-off analysis between the normalized slowness norm and the data residual norm for a set of smoothing parameters using the optimal damping parameter of 300. Because the smoothing parameter is applied to constrain the slowness, only the norm of slowness is used for the analysis of optimal smoothing parameter. The optimal smoothing parameter is selected around 20. In (f), the more accurate WCC data is weighted more than the catalog data from iteration 7, resulting in a stair-step pattern at iteration 7.

3. Tomographic details

Fig. 1c shows the Cartesian coordinate system and the horizontal grid setting used for the inversion. The grid nodes in the depth direction are positioned at $Z = 0, 2, 2.96, 3.5, 4, 5, 6, 7, 8, 9, 10, 13$, and 25 km, respectively. Note that the depth of $Z = 0$ km represents the depth of sea level. Figs. 3a–c show initial earthquake locations and 1-D V_p model. The initial 1-D V_p model is constructed by averaging the V_p model of the low-velocity fault zone determined by the active-source refraction study, and the V_p models 10 km north and south of the active fault trace (Roland et

al., 2012). The initial V_p/V_s value is 1.73. The initial V_s model is converted from initial V_p and V_p/V_s models.

It is known that performing tomographic inversion with better initial earthquake locations and velocity models can always result in better results. Thus, our inversion strategy is first to use the original DD tomography method of Zhang and Thurber (2003) to invert earthquake locations, V_p and V_s models, which are then used as the starting models for the new consistency-constrained DD tomography to determine our final results.

We perform the inversion with a hierarchical weighting scheme for the catalog and WCC data (Zhang and Thurber, 2003). Regu-

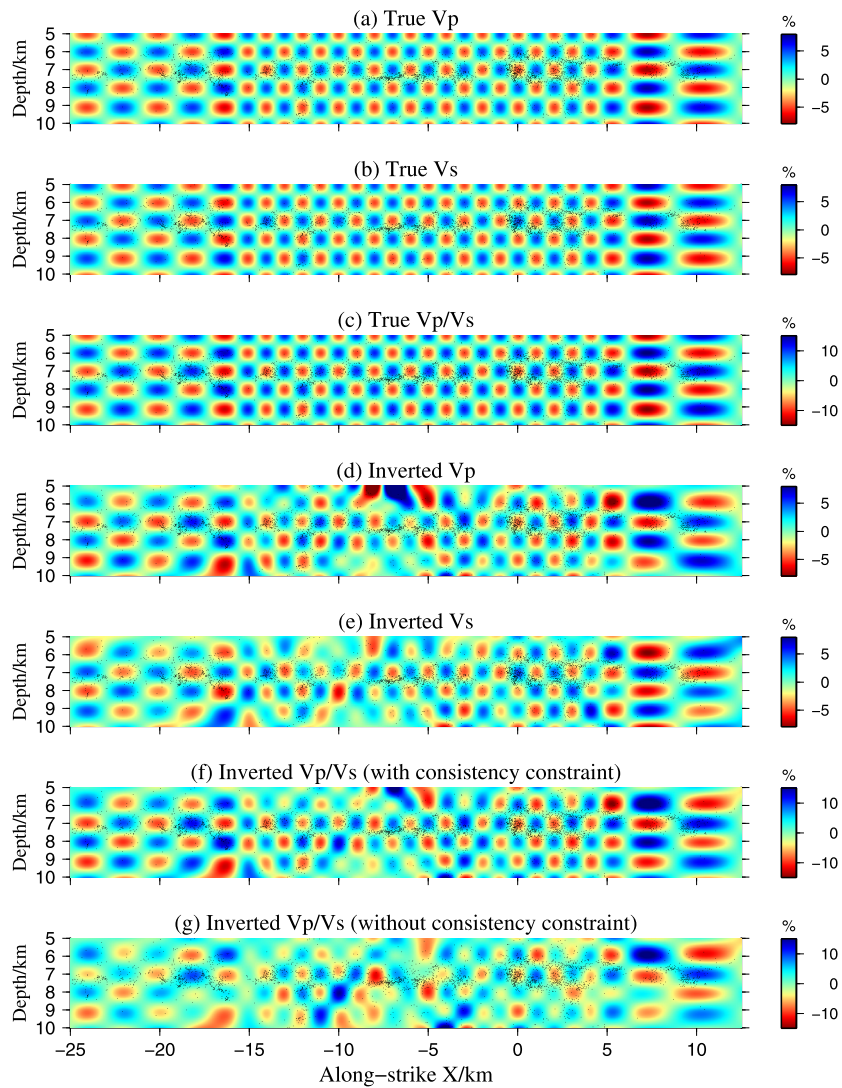


Fig. 4. Checkerboard resolution test. (a–c) The input “true” V_p , V_s , and V_p/V_s checkerboard models used to generate synthetic data. (d–f) Inverted V_p , V_s , and V_p/V_s checkerboard models from the inversion with consistency constraint. (g) Inverted V_p/V_s model from the inversion without consistency constraint. All these plots are at the cross-section of $Y = 2$ km. Earthquakes (dots) between $Y = 1.5$ km and $Y = 2.5$ km are shown. The true V_p and V_s models consist of positive and negative 5% velocity anomalies with respect to the initial 1-D velocity models at alternating grid nodes. Checkerboard patterns for true V_p and V_s models are set to be opposite at the same grid node so that the checkerboard pattern of true V_p/V_s model can alternate with positive 10.5% and negative 9.5% anomalies.

lariization parameters, including smoothing and damping factors, which are used to stabilize the inversion, are selected with a trade-off analysis (Figs. 3d–e). Throughout inversion iterations, data residuals for both the catalog and the WCC data converge well (Fig. 3f).

For earthquake relocations, we estimate relative location uncertainty with a bootstrapping resampling method (Guo and Zhang, 2017), and absolute location uncertainty with a restoration synthetic test (see Supplementary Material). To estimate the resolution of velocity models, we perform two synthetic tests, including a checkerboard test and a restoration test (Zhao and Hasegawa, 1993), both of which have been widely used in seismic tomography. For the checkerboard test, we create “true” V_p , V_s , and V_p/V_s models with checkerboard patterns by adding positive and negative velocity anomalies to initial 1-D models at alternating grid nodes (Figs. 4a–c). Then these true models are used to generate synthetic absolute and differential times that have the same distribution as the real data. The synthetic data are then used for inversion starting from initial 1-D models. The recovered models at the cross-section of $Y = 2$ km (Figs. 4d–f) show that the fault-zone structure at depths of 6 to 10 km below sea level can be

well resolved. The restoration resolution test shows that the key model features resulting from the real data inversion, which will be discussed in the following sections, can be well recovered and are thus reliable (see Supplementary Material). In addition to these two synthetic tests, we also check the fitting of the active-source data, which further indicates that our velocity model is reliable (see Supplementary Material).

4. Validation of the V_p/V_s model consistency-constrained DD tomography method

We test the performance of the new consistency-constrained DD tomography method compared to the original method of Zhang et al. (2009) by analyzing both the synthetic checkerboard test and the real data inversion.

Figs. 4f and 4g show the comparison of the inverted V_p/V_s models from two checkerboard tests with and without the new consistency constraint. It can be seen that the new method can better resolve the amplitude of V_p/V_s anomalies. Moreover, some areas that have poor resolutions from the inversion with the orig-

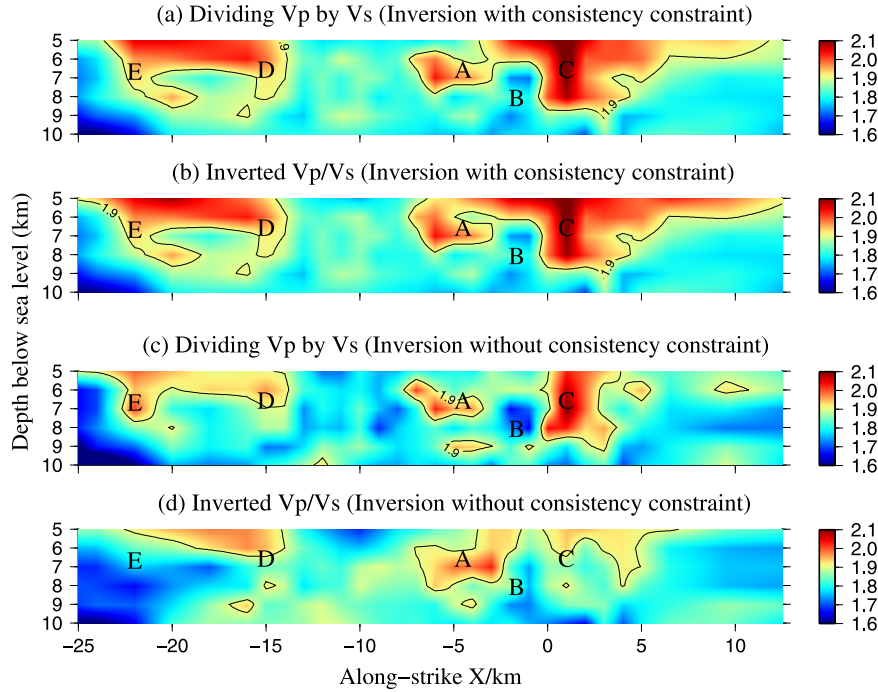


Fig. 5. Comparison between the inverted V_p/V_s models (**b, d**) and the V_p/V_s model obtained by dividing the inverted V_p by the inverted V_s (**a, c**), from the inversion with (**a, b**) and without (**c, d**) the consistency constraint, at the vertical cross-section of $Y = 2$ km. Zones A–E shown in Fig. 8 are also labeled. Note that compared to models shown in Fig. 8, these models result from the inversions starting from 1-D velocity model.

inal method, e.g. near $X = -5$ km and $X = -15$ km, can be well resolved with the new method.

Figs. 5b and 5d show the comparison of the inverted V_p/V_s models from two real data inversions with and without the consistency constraint. To make fair comparison, both inversions start from the same earthquake locations and 1-D velocity models, and use the same inversion parameters. Overall, the inverted V_p/V_s models from these two inversions are similar. However, the inverted V_p/V_s model from the new method can reveal more detailed structures, e.g. some small-scale anomalies which are smeared in the inverted V_p/V_s model from the original method, indicating the new method can determine higher-resolution V_p/V_s model. Furthermore, the inverted V_p/V_s model (Fig. 5b) and the V_p/V_s model obtained by dividing V_p model by V_s model (Fig. 5a) from the new method are much more consistent compared to the results from the original method (Figs. 5c–d). The consistency between the inverted V_p/V_s model and the model by dividing V_p model by V_s model indicates the consistency of model anomalies in the inverted V_p , V_s , and V_p/V_s models, which will be very helpful for interpreting model anomalies.

5. Results

As mentioned in section 3, our final results, shown in Figs. 6–9, are determined by starting the consistency-constrained DD inversion from the 3-D velocity models determined by the original DD method of Zhang and Thurber (2003). However, both inversion results starting from 1-D and 3-D models are very comparable (Fig. 5b and 8c), also indicating that the new method is very stable with regard to using different initial velocity models.

We separate the fault into 4 patches (Fig. 6a) according to different features in velocity anomalies and earthquake activity, which will be described below. Patch 4, where the December swarm occurred, is close to the tomographic boundary, therefore, we only focus on patches 1, 2, and 3. In the following sections, depth values are relative to sea level at depth of $Z = 0$ km unless otherwise specified.

5.1. Earthquake relocations

Figs. 6a–b show the map view and along-strike vertical cross-sections of earthquake relocations with small location uncertainties estimated with bootstrapping analysis. Fig. S2 shows all relocations, regardless of location uncertainty. Compared to initial catalog locations (Figs. 3a–b) and previous relocations (McGuire et al., 2012; Froment et al., 2014), our relocations from the joint inversion with P- and S-wave arrival data as well as the WCC data are more concentrated in both horizontal and vertical views, suggesting that the relative locations between events are greatly improved, especially for the events within clusters. Absolute locations are also well resolved due to the utilization of absolute arrival times and the joint inversion. Improved earthquake locations outline a very clear delineation of the active fault trace at about $Y = 2$ km, with the seismicity in the western area gradually deflecting to the south (Fig. 6a).

The earthquakes that occurred after the mainshock have a tendency to be systematically deeper than the pre-mainshock background seismicity (Figs. 6b–c). Froment et al. (2014) observed a significant velocity reduction below G08 in patch 1 (−2% to −6%) during the foreshock period and following the mainshock. A similar reduction was also observed below G06 in patch 2 (−4% to −10%) following the mainshock. This means that the velocity model inverted with all the data is an average of the possible temporal velocity changes for the period and should generally be slower than the actual velocity model in patches 1 and 2 during the period before the foreshocks. Background earthquakes in patches 1 and 2 would therefore be shifted ∼0.5 km shallower. By contrast, the foreshocks and the earthquakes that occurred after the M6 there would be ∼0.5 km deeper, which is consistent with the result shown in Figs. 6b–c. Froment et al. (2014) did not observe a velocity reduction in patch 3 due to the data gap before the mainshock, but based on the systematic depth differences between background seismicity and the earthquakes after the mainshock (Figs. 6b–c), there could also be a velocity reduction in patch 3 following the mainshock.

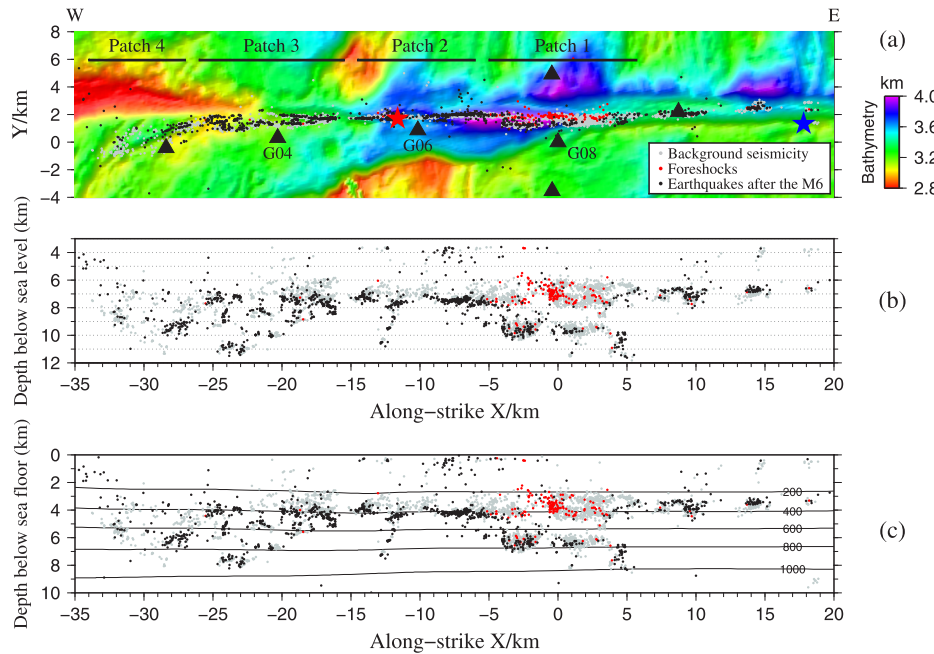


Fig. 6. Map view (a) and along-strike vertical cross-section (b and c) of the earthquake relocations. Only earthquakes with bootstrapping location uncertainties less than 0.2 km in the X and Y directions and 0.3 km in the Z direction are shown. In (b), earthquake depths are relative to sea level. In (c), earthquake depths are converted to be relative to the sea floor, which also takes the variation of topography into account. The isotherms (labeled in Celsius) of the thermal model from Roland et al. (2012) are shown in (c). Patches 1–4 are defined based on different features in velocity anomalies and earthquake activity (see the description in the main text).

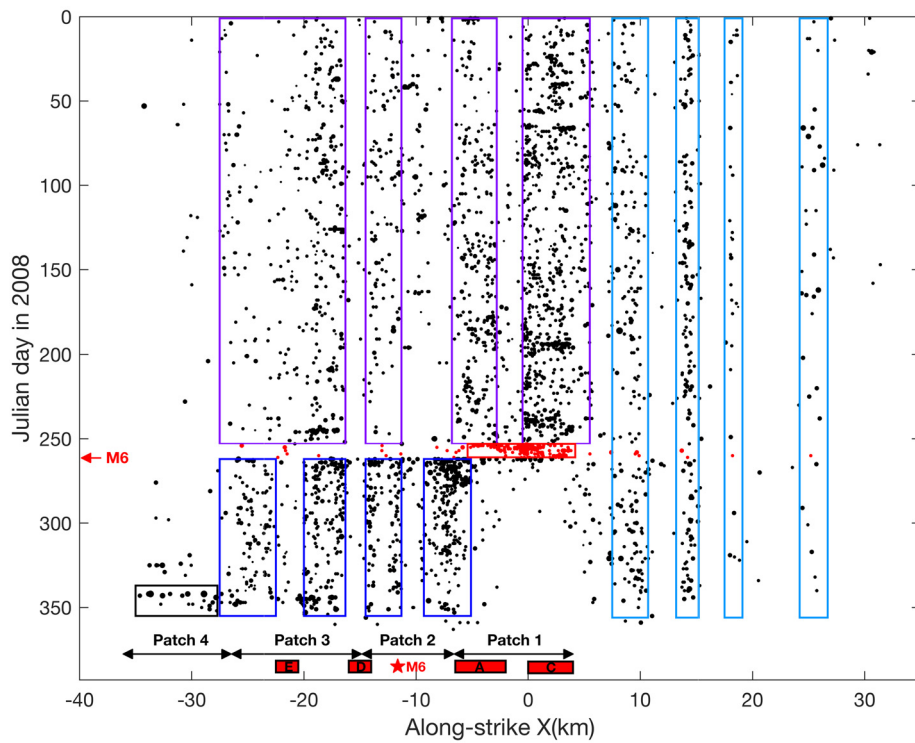


Fig. 7. Temporal and spatial (along-strike) evolution of the 1-year-long seismicity (dots) at depths of ~6–8 km below sea level (i.e. ~3–5 km below the sea floor). Red dots represent earthquakes during the foreshock period. Dot sizes are slightly adjusted based on their earthquake magnitudes. The 2008 M6 earthquake is marked by the red star and red arrow in the horizontal and vertical axes, respectively. Colored open rectangles are used to define earthquake segmentations in space and time. Red solid rectangles indicate high- V_p/V_s anomaly zones shown in Fig. 8 and their along-strike lengths represent the lengths of these anomalies in the seismogenic depth range of $Z = 6$ to 8 km below sea level. Patches 1–4 are marked.

Overall, most earthquakes are generated at depths of ~3–5 km below the sea floor (i.e. ~6–8 km below sea level) (Figs. 6b–c). However, there exist a lot of deep earthquakes at depths of ~5–8 km below the sea floor in patches 1, 3, and 4, compared to patch 2 (Fig. 6b–c). In comparison, McGuire et al. (2012) deter-

mined much deeper seismicity (~7–11 km below the sea floor) in patch 1, which could explain some observed large S-P times (see Fig. 3 in McGuire et al., 2012) assuming a constant V_p/V_s of 1.73. Our joint inversion result indicates that the large S-P times should be attributed to both the deeper extent of the seismicity and high

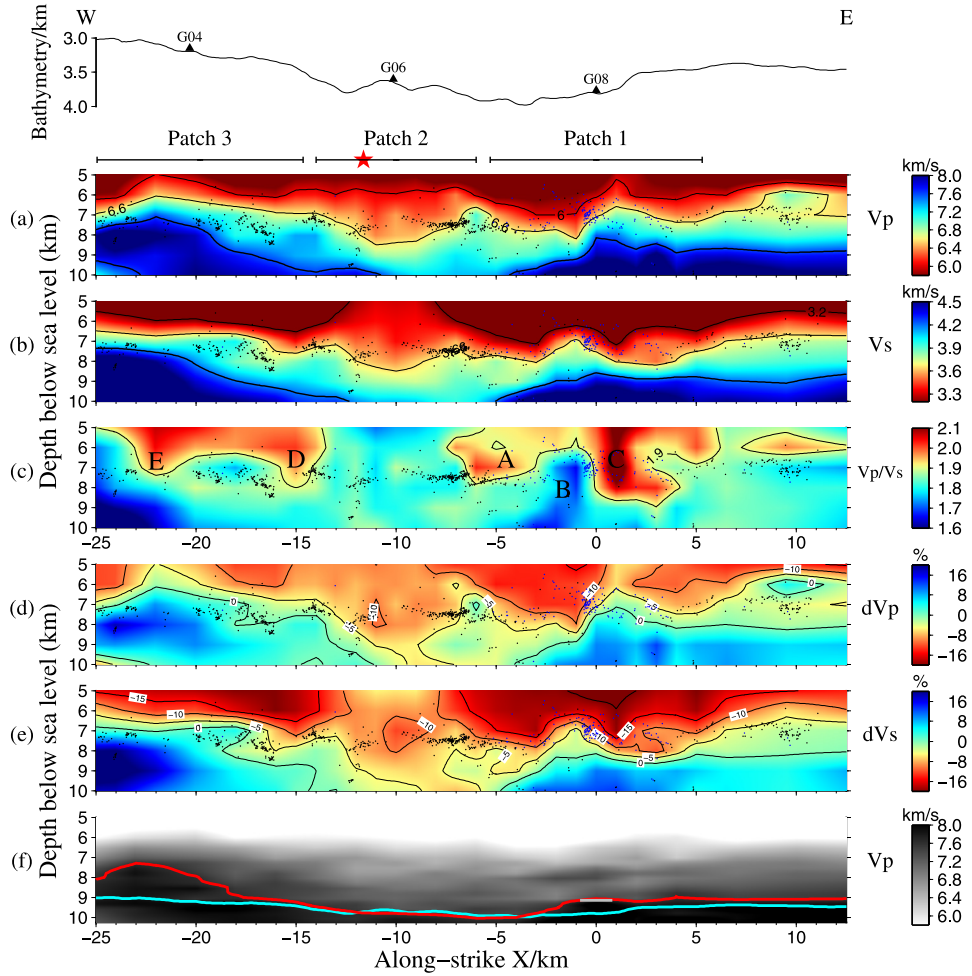


Fig. 8. (a) V_p , (b) V_s , (c) V_p/V_s , (d) dV_p and (e) dV_s models as well as (f) Moho variations at the vertical cross-section of $Y = 2$ km from $X = -25$ to 12.5 km. In the top, the local bathymetry profile along this cross-section is shown and the surrounding stations G04, G06 and G08 are projected onto it and labeled. The V_p model is contoured at 6.0, 6.6 and 7.6 km/s. The V_s model is contoured at 3.2, 3.66 and 4.2 km/s. The V_p/V_s model is contoured at 1.9. Both dV_p and dV_s (%) are contoured at $-20, -15, -10, -5, 0, 5, 10, 15$ and 20. Red star represents the 2008 M6 mainshock (McGuire et al., 2012). Foreshocks and the earthquakes after the mainshock from $Y = 1.5$ to 2.5 km are represented by blue and black dots, respectively. Only earthquakes with bootstrapping location uncertainties less than 0.2 km in the X and Y directions and 0.3 km in the Z direction are shown. In (f), the Moho discontinuity (red curve) is inferred from the 7.6 km/s contour of the V_p model resulting from a separate inversion with denser grid nodes in depth and coarser grid nodes in the horizontal directions. The cyan curve represents the normal Moho discontinuity by assuming the crustal thickness of 6 km. The gray line at $X = 0$ km represents the Moho discontinuity estimated by Roland et al. (2012) from a wide-angle refraction study crossing the fault.

V_p/V_s structures in patch 1 (see section 5.3), rather than much deeper extent of the seismicity alone. In addition, there also exist some shallow earthquakes at depths less than 2 km below the sea floor (Fig. 6 and Fig. S2b). Due to their large location uncertainties (Figs. S2c-d), however, we will not focus on these shallow earthquakes in this paper.

5.2. Temporal and spatial evolution of the year-long seismicity

McGuire et al. (2012) have shown the temporal and spatial (along-strike) evolution of the year-long seismicity using the complete event catalog. By using higher-resolution relocations, we can more clearly show the evolution pattern of the seismicity at seismogenic depths of $\sim 3\text{--}5$ km below the sea floor (i.e. $\sim 6\text{--}8$ km below sea level) (Fig. 7). It is worth noting that, although the earthquakes used in this study are partially selected from the catalog used by McGuire et al. (2012), the evolution pattern should still be representative because the selection criteria are not related to the earthquake location and the occurrence time.

From 1 January to 9 September 2008, the fault from $X = -30$ to 30 km experienced a lot of background seismicity. Among all patches, patch 1 experienced the highest rate of back-

ground seismicity, as shown in McGuire et al. (2012). Then, patch 1 culminated in a large swarm of foreshocks within a 1-week period from 10 September (day 254) to 17 September (day 261), which was immediately terminated on 18 September (day 262) when the mainshock occurred on patch 2. For this reason, patch 1 is also called the foreshock zone. After the mainshock, patches 2 and 3 experienced a high rate of seismicity for a few weeks and then gradually recovered to the level of the background seismicity. After the mainshock, the seismicity in patch 1 decreased to a very low level at depths of $\sim 3\text{--}5$ km (Figs. 6c and 7) but was relatively active in the deep area at depths of $\sim 5\text{--}7$ km below the sea floor (Fig. 6c). The seismicity in patch 1 following the mainshock was much weaker compared to patch 2 (Fig. 6c), thus, patch 1 acted as a mainshock rupture barrier. On 10–17 December (day 345–352), the westernmost patch 4 experienced an earthquake swarm, which can be better viewed from the more complete catalog of McGuire et al. (2012).

It is clear that the earthquakes at depths of $\sim 3\text{--}5$ km below the sea floor preferentially occur in specific patches (some are sub-patches within the three large patches 1–3) along the fault during specific periods, as delineated by a series of the colored rectangles

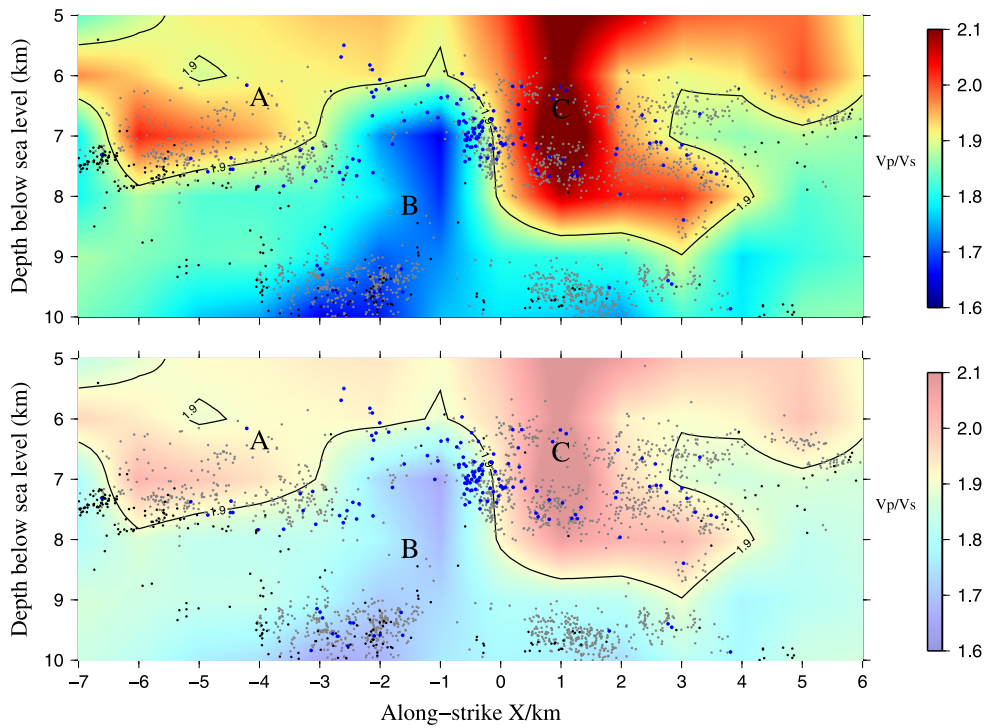


Fig. 9. Zoom-in view of V_p/V_s anomalies and earthquake locations at the cross-section of $Y = 2$ km from $X = -7$ to 6 km. In the bottom figure, the V_p/V_s image is set to be with low intensity of illumination so that the spatial distribution of earthquakes can be seen more clearly. Background earthquakes, foreshocks and earthquakes after the mainshock from $Y = 1$ to 2.5 km are shown as gray, blue and black dots, respectively. Note that compared to Fig. 8c, deep earthquakes, which are located between $Y = 1$ and 1.5 km, are also included.

in Fig. 7. By contrast, the areas between these patches have no or very weak seismicity.

5.3. Velocity models

In this section, we describe V_p , V_s , and V_p/V_s models at the along-strike cross-section of $Y = 2$ km, shown in Figs. 8 and 9. In addition, Fig. 8 shows V_p and V_s differences with respect to the reference 1-D V_p and V_s models. The reference V_p model (Fig. S3) is derived from averaging two 1-D velocity profiles located 10 km south and north of G3 (Roland et al., 2012), which can be used as a proxy for the normal EPR crustal V_p model around G3. The reference V_s model is derived by assuming a constant V_p/V_s of 1.8, which is a mean EPR crustal V_p/V_s estimated from an ambient noise study (Yao et al., 2011). We also approximately estimate the Moho depth with the V_p contour of 7.6 km/s (Detrick et al., 1993) using another inversion with denser grid intervals in depth and coarser grid interval in the Y direction. This parameterization allows for a higher resolution in depth and thus can be used to better estimate the Moho discontinuity (see supplementary material).

5.3.1. Patch 1

Patch 1 is thinner than the average 6-km thick oceanic crust (Fig. 8f), and shows a strong structural segmentation. Three V_p/V_s anomaly zones (A, B, C) can be identified from high-resolution velocity models (Fig. 8). Compared to the reference crustal model, zone A ($X = -7$ to 3 km, $Z = 5$ to 8 km) shows low V_p ($\sim -5\%$ to -15%), low V_s ($\sim -10\%$ to -20%), and high V_p/V_s (~ 1.9); zone B ($X = -3$ to 0 km, $Z = 6$ to 9 km) shows low V_p ($\sim -5\%$ to -13%), low V_s ($\sim 0\%$ to -10%), and a relatively low V_p/V_s (< 1.75); and zone C ($X = 0$ to 4 km, $Z = 5$ to 9 km) shows low V_p ($\sim 0\%$ to -10%), low V_s ($\sim -10\%$ to -20%), and high V_p/V_s (~ 2.0).

5.3.2. Patch 2

Patch 2 shows normal crustal thickness (i.e. ~ 6 km), which is ~ 1 km deeper than adjacent patches 1 and 3 (Fig. 8f). In the deep part ($Z > 7.5$ km), patch 2 has lower V_p and V_s values than its neighboring patches at the same depth, which is simply due to the crustal uplift beneath patches 1 and 3. In the shallow part ($Z < 7.5$ km), however, V_s is actually much higher than the neighboring patches. The V_p/V_s model in patch 2 from $Z = 5$ to 8 km is normal or slightly high (~ 1.8) but much lower than the neighboring high- V_p/V_s zones.

5.3.3. Patch 3

In patch 3, there are two V_p/V_s anomalous zones D and E at depths of $Z = 5$ to 8 km, associated with low V_p (~ 0 to -10%), low V_s ($\sim -10\%$ to -20%) and high V_p/V_s (> 1.9). Although these two zones are connected in the shallow depth ($Z < 6$ km), they are separate at seismogenic depths ($Z = 6$ to 8 km) (Fig. 8c). The crust in patch 3 is thinner than the average 6-km crustal thickness.

It should be noted that the 1-D reference model, which is used to represent normal crustal velocity, is not very suitable for the calculation of velocity difference models in patches 1 and 3. As indicated by the shallower Moho depths revealed by the inversion (Fig. 8f) compared to the depth of $V_p = 7.6$ km/s in the 1-D reference model (Fig. S3), the 1-D reference model is likely underestimated in patches 1 and 3. Thus the velocity differences in patches 1 and 3 shown in Figs. 8d–e are overestimated and should be smaller, which means that the amplitude of the velocity decrease of zones A–E should be larger and that the low-velocity structures should be more clearly at the bottom boundaries of zones B and E.

6. Interpretations and discussions

In this section, we will interpret velocity structures in patches 1–3 and discuss the relationship between structural variations and

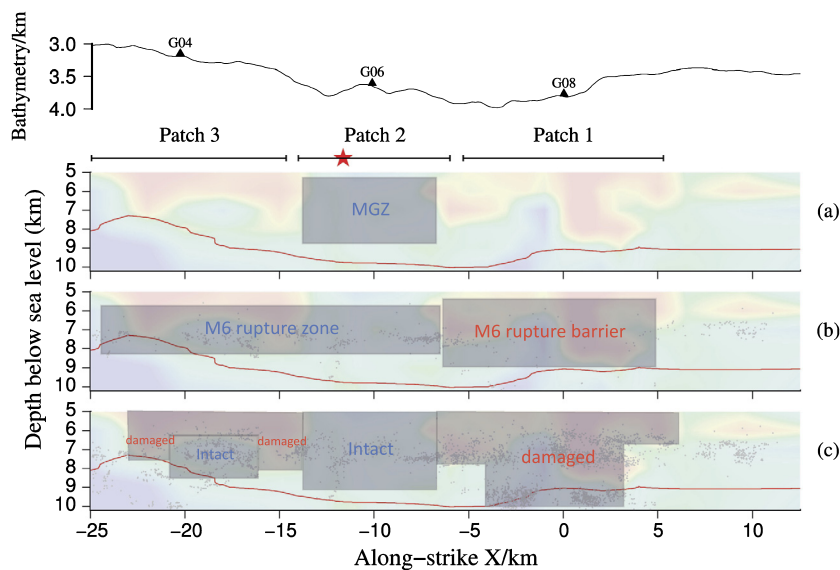


Fig. 10. Summary Cartoon of main conclusions on along-strike variations in earthquake rupture properties and fault-zone material properties. (a) The shaded area represents the M6 mainshock generation zone (MGZ). (b) Two shaded areas represent the mainshock rupture zone and the mainshock rupture barrier zone. Earthquakes after the mainshock from $Y = 1.5$ to 2.5 km, with small bootstrapping location uncertainties, are shown as gray dots. (c) Spatial distribution of intact and damaged zones that are discussed in Section 6. Earthquakes in the whole year from $Y = 1$ to 2.5 km, with small bootstrapping location uncertainties, are shown as gray dots. The background image with low intensity of illumination represents the V_p/V_s model at the cross-section of $Y = 2$ km (i.e. Fig. 8c). The red line represents the Moho. The seafloor variation is shown in the top.

earthquake behaviors along strike. Our main conclusions are illustrated in a cartoon figure (Fig. 10).

6.1. Along-strike variations in material properties

The active-source wide-angle refraction study across patch 1 (Roland et al., 2012) imaged a low-velocity fault zone extending through the entire crust with V_p reduced by 10–20%. Similarly, the P-wave tomographic study using the earthquake data also showed a low-velocity fault zone in patch 1 (Froment et al., 2014). Based on the analysis of the gravity data (Pickle et al., 2009), it is most likely that the low velocity in patch 1 is caused by the enhanced fluid-filled porosity (1.5–8%) rather than serpentinization (Roland et al., 2012). Compared to these previous V_p models, our V_p/V_s model shows more detailed structural variations in patch 1 (Figs. 8 and 9).

For zones A and C, low V_p , low V_s , and high V_p/V_s values, can be well explained by enhanced fluid-filled porosity, which would cause V_s decreasing more than V_p (Kuster and Toksöz, 1974; Takei, 2002). Different amplitudes of V_p/V_s anomalies in zones A and C (Fig. 8c) could be caused by different degrees in porosity and/or pore shape (e.g. aspect ratio) (Kuster and Toksöz, 1974; Takei, 2002). In addition, if fluids existed, a small amount of serpentine minerals probably could exist as well, although it is not expected to be the main cause of the velocity anomalies (Roland et al., 2012).

Additional evidence for the existence of fluids in patch 1 comes from the deep extension of the seismicity (Fig. 6c) in this patch. Oceanic seismogenic depths are generally shallower than the 600 °C isotherm (Abercrombie and Ekström, 2001; McKenzie et al., 2005). Roland et al. (2012) predicted the 600 °C isotherm of the G3 segment corresponds to a depth of ~4 km below the sea floor for a half-space cooling model, but can increase to ~5–6 km for a hydrothermal cooling model. Although earthquake depth extension in patch 1 is still deeper than the prediction from the hydrothermal model (Fig. 6c), it could be explained if a certain degree of local fluid circulation is considered for a cooler model (McGuire et al., 2012; Roland et al., 2012).

The occurrence of deep seismicity at the bottom of zone B implies the deep area of patch 1 to be damaged and filled with fluids. Different from zones A and C, however, zone B shows relatively low V_p/V_s (Fig. 9). Based on the two-phase effective media calculation with different rock porosities, pore fluids, and pore shapes (Kuster and Toksöz, 1974; Takei, 2002), a reduction of V_p/V_s needs the aspect ratio of cracks to be large and/or a part of pore spaces to be composed of gas. Considering the high pressure in depth, the existence of pore gas seems unlikely and thus large pore aspect ratio may be a better explanation. However, if the super-critical or near-critical hydrothermal fluids are present in depth, which is possible within the young, hot GTF, the transition from liquid to vapor may happen due to the decrease of pore-fluid pressure in response to fault dilatancy (Geli et al., 2014), which also could result in relatively low V_p/V_s value.

Compared to patch 1 where most areas at depths of 6–11 km below sea level are damaged (Fig. 10), patch 2 shows different velocity structure. Froment et al. (2014) found that the mean V_p value in patch 2 was higher than the values in patches 1 and 3 and thus suggested that patch 2 was composed of relatively intact gabbro and peridotite rocks. Our higher-resolution models (Fig. 8) also show that overall, patch 2 has higher V_p and V_s values compared to its adjacent patches (note that as mentioned in section 5.3.2, the lower velocity in the deep area of the patch 2 compared to patches 1 and 3 is due to the crustal uplift in patches 1 and 3 rather than the damage of this area). The V_p/V_s value of patch 2 is ~1.8. For the undamaged gabbro in the middle and lower oceanic crust, the normal V_p/V_s values range from ~1.8 to ~1.85, with variations resulting from differing olivine content in the gabbro (Christensen, 1996). The ambient noise study also suggested the mean EPR crustal V_p/V_s value to be ~1.8 (Yao et al., 2011). Thus, our result confirms that patch 2 is likely to be composed of relatively intact rocks (Fig. 10).

Similar to zones A and C, zones D and E in patch 3 show low V_p , low V_s , and high V_p/V_s anomalies and are suggested to be damaged with high fluid-filled porosity (Figs. 8 and 10). Same as patch 1, additional evidence for the existence of fluids in patch 3 comes from enhanced earthquake depths (Fig. 6c). Between zones

D and E ($X = -20$ to -16 km), at seismogenic depths of ~ 6 – 8 km below sea level, an area similar to the patch 2 is imaged with relatively normal V_p , V_s , and V_p/V_s , indicating relatively intact rocks there (Figs. 8c and 10).

6.2. Structural control on the generation and propagation of the mainshock

High-resolution relocations and velocity models reveal some relationships between structural variations and large earthquakes at seismogenic depths of ~ 6 to 8 km below sea level. The 2008 M6 mainshock occurred in patch 2 where we image a relatively intact fault zone. By contrast, patch 1 (the inferred rupture barrier) to the east, shows two large-scale, highly damaged zones, and patch 3 to the west, shows two small-scale damaged zones. Although there also exists a small-scale (~ 4 -km-long) zone composed of relatively intact rocks in patch 3, we speculate that all the other quasiperiodic M6 earthquakes (red stars in Fig. 1b) are nucleated on the ~ 8 -km-long patch 2, same as the 2008 M6 mainshock. With weak pre-mainshock seismicity (Fig. 7), patch 2 could be relatively locked during the interseismic period to accumulate stress, which is released quasiperiodically by M6 earthquakes associated with coseismic damage of the fault zone, as evidenced by the coseismic velocity decrease (Froment et al., 2014). Thus, we suggest that a relatively intact fault patch at seismogenic depths with sufficient length (~ 8 -km-long) is necessary for the stress build-up for large M6 earthquakes on the GTF (Figs. 10a and 10c).

Intense foreshocks associated with some aseismic events in patch 1 could cause the fault zone to undergo dilatant strengthening, and increase the porosity of the fault zone, as evidenced from the velocity decrease during the foreshock period (McGuire et al., 2012; Froment et al., 2014). As suggested by McGuire et al. (2012), the ability of patch 1 to stop the subsequent mainshock rupture may be caused by the fault dilatant strengthening (Segall et al., 2010; Segall and Bradley, 2012) and a small amount of serpentine minerals within the damaged zones of patch 1. In comparison, intensive seismicity in patch 3 after the mainshock indicated that the M6 mainshock was likely able to rupture through not only the ~ 8 -km-long patch 2 but also the ~ 10 -km-long patch 3 (Fig. 7 and 10b) (McGuire et al., 2012). Compared to patch 1 where most areas are damaged at seismogenic depths, the small size of damaged zones D and E (~ 2 -km-long) within patch 3 may explain this observation (Figs. 7 and 10b–c), indicating that the size of the damaged zone plays an important role in the rupture propagation of large M6 earthquakes on the GTF.

Global observations of earthquakes on RTFs suggest a low seismic coupling ($\sim 15\%$) (Bird et al., 2002; Boettcher and Jordan, 2004). Considering the similar scaling relationship between the GTF and other RTFs (Boettcher and Jordan, 2004), our result also further confirms the hypothesis of Froment et al. (2014) that the existence of fluid-filled, damaged zones with different scales is likely responsible for the deficit of seismic slip on global RTFs.

6.3. Structural control on small earthquakes

High-resolution relocations and velocity models reveal some relationships between structural variations and small earthquakes. Overall, small earthquakes along strike are highly segmented into different clusters (Figs. 6b and 7), among which some horizontal, slip-parallel earthquake streaks can be seen, e.g. the one around $X = -7$ km shown in Fig. 6b. Such spatial distribution of small earthquakes has been observed in continental strike-slip faults, and is suggested to be structural in origin (Rubin et al., 1999; Waldhauser et al., 1999, 2004; Schaff et al., 2002; Waldhauser and Ellsworth, 2002).

In patch 1, most background earthquakes and foreshocks tend to occur near the boundaries of the anomalous zones A, B, and C (Fig. 9), indicating that the nucleation and spatial distribution of small earthquakes in patch 1 is structurally controlled. Following the suggestion from McGuire et al. (2012) that the week-long foreshocks were likely triggered by a large aseismic creep event in patch 1, we further suggest that this aseismic event may be generated in zone B, which showed very weak seismicity throughout the 2008 deployment at depths of 6 to 9 km. As a result, the stress perturbations from the aseismic event could be effectively transferred around zone B to trigger foreshocks. Most foreshocks were concentrated into a very narrow area near $X = -0.5$ km between zones B and C (Fig. 9), indicating highest stress concentration there.

In addition to the explanation that foreshocks were triggered by the stress perturbations from aseismic events, Geli et al. (2014) suggested that the decrease of the pressure of the super-critical or near-critical hydrothermal fluids in response to fault dilatancy could significantly increase the fluid compressibility, which could trigger an unstable phase of fault slip. This kind of fluid-related process in zone B may also trigger foreshocks, especially near the boundaries between zone B and its surrounding zones, where stresses were concentrated.

In addition, the deep area of zone B ($Z = 9$ to 10 km) experienced relatively active seismicity after the mainshock compared to the zone just above it ($Z = 6$ to 8 km), though this seismicity was much weaker than its pre-mainshock level (Fig. 9). This deep area has relatively low V_p/V_s , implying a different earthquake generation mechanism there compared to the shallower area just above it.

In patch 2, two separate earthquake clusters, located near $X = -10$ km, occurred following the mainshock (Figs. 7 and 8), which may be related to the coseismic damage, as evidenced by the coseismic velocity decrease observed in this patch (Froment et al., 2014). In patch 3, damaged zones D and E have weak seismicity within them, but have some earthquake clusters surrounding them (Figs. 7 and 8).

Thus, we suggest that structural variations from damaged zones with fluid-filled porosity to undamaged (or much less damaged) zones control the nucleation and spatial distribution of small earthquakes (Figs. 7 and 10c). Highly segmented seismicity in the spatial and temporal evolution of the 2008 seismic catalog (Fig. 7) indicates even stronger structural variations along strike than what we have imaged.

7. Conclusions

We have determined high-resolution earthquake locations, V_p , V_s , and V_p/V_s models along the G3 segment of the GTF, which help to reveal strong fault structural variations of different scales from fluid-filled damaged zones to undamaged zones. Our results further confirm some inferences of previous studies and also reveal more details on the relationship between structural variations and earthquake behaviors along the fault (Fig. 10).

The 2008 M6 mainshock was generated within a ~ 8 -km-long patch with high V_p , high V_s and normal V_p/V_s values. As inferred by Froment et al. (2014), this patch is likely to be composed of relatively intact rocks. The neighboring patch to the east consists of several damaged zones with varying V_p/V_s values. This confirms the interpretation from McGuire et al. (2012), Roland et al. (2012), and Froment et al. (2014) that most areas in this ~ 10 -km-long patch are likely damaged at seismogenic depths, which can well explain its ability of stopping mainshock rupture propagation. The neighboring patch to the west cannot generate large earthquakes, which is suggested by our model to be due to the limited size (~ 4 -km-long) of intact seismogenic zone. This patch also can-

not stop large earthquake rupture propagation, which is suggested to be due to the limited size (~ 2 -km-long) of damaged zones at seismogenic depths. Along the strike, small earthquakes are highly segmented into many clusters, which preferentially occur within the zones with relatively normal V_p/V_s values or around the boundaries between high and normal/low V_p/V_s anomalies.

Thus, strong structural variations in material properties, as evidenced by earthquake locations and velocity models, control the behaviors of large and small earthquakes along the GTF, and is likely responsible for the deficit of seismic slip on global RTFs. The application of high-resolution imaging to the GTF shows that by characterizing fault-zone structures with V_p , V_s , and especially V_p/V_s , we can gain a much better understanding of earthquake behavior and fault mechanical behavior.

Acknowledgements

We thank Jeff McGuire for providing the catalog dataset and for very helpful discussions on the result and interpretation. We thank Louis Geli and two anonymous reviewers for their very insightful comments and suggestions that helped us significantly improve the paper. All the waveform data used was acquired and made available by WHOI, and has been archived at the IRIS Data Center. This research is partly supported by the National Key Research and Development Project of China under grant number 2016YFC0600302 and by National Natural Science Foundation of China under grant number 41474039.

Appendix A. Supplementary material

Supplementary material related to this article can be found online at <https://doi.org/10.1016/j.epsl.2018.07.037>.

References

- Abercrombie, R., Ekström, G., 2001. Earthquake slip on oceanic transform faults. *Nature* 410, 74–77.
- Bird, P., Kagan, Y.Y., Jackson, D.D., 2002. Plate tectonics and earthquake potential of spreading ridges and oceanic transform faults. In: *Plate Boundary Zones*. American Geophysical Union, pp. 203–218.
- Boettcher, M.S., Jordan, T.H., 2004. Earthquake scaling relations for mid-ocean ridge transform faults. *J. Geophys. Res., Solid Earth* 109 (B12).
- Christensen, N.I., 1996. Poisson's ratio and crustal seismology. *J. Geophys. Res.* 101 (B2), 3139–3156. <https://doi.org/10.1029/95JB03446>.
- Detrick, R.S., White, R.S., Purdy, G.M., 1993. Crustal structure of North Atlantic fracture zones. *Rev. Geophys.* 31 (4), 439–458.
- Du, W.X., Thurber, C.H., Eberhart-Phillips, D., 2004. Earthquake relocation using cross-correlation time delay estimates verified with the bispectrum method. *Bull. Seismol. Soc. Am.* 94 (3), 856–866.
- Froment, B., McGuire, J.J., Hilst, R.D., Gouédard, P., Roland, E.C., Zhang, H., Collins, J.A., 2014. Imaging along-strike variations in mechanical properties of the Gofar transform fault, East Pacific Rise. *J. Geophys. Res., Solid Earth* 119 (9), 7175–7194.
- Geli, L., Piau, J.M., Dziak, R., Maury, V., Fitzenz, D., Coutellier, Q., Henry, P., Broseta, D., Steele-MacInnis, M., Diesner, T., 2014. Seismic precursors linked to highly compressible fluids at oceanic transform faults. *Nat. Geosci.* 7 (10).
- Gouédard, P., Seher, T., McGuire, J.J., Collins, J.A., van der Hilst, R.D., 2014. Correction of ocean-bottom seismometer instrumental clock errors using ambient seismic noise. *Bull. Seismol. Soc. Am.* 104 (3), 1276–1288.
- Guo, H., Zhang, H., 2017. Development of double-pair double difference earthquake location algorithm for improving earthquake locations. *Geophys. J. Int.* 208 (1), 333–348.
- Harris, R.A., 2017. Large earthquakes and creeping faults. *Rev. Geophys.* 55 (1), 169–198.
- Ide, S., Beroza, G.C., Shelly, D.R., Uchide, T., 2007. A scaling law for slow earthquakes. *Nature* 447 (7140), 76–79.
- Kuster, G.T., Toksöz, M.N., 1974. Velocity and attenuation of seismic waves in two-phase media: Part I. Theoretical formulations. *Geophysics* 39 (5), 587–606.
- Maeda, N., 1985. A method for reading and checking phase times in autoprocessing system of seismic wave data. *Zisinjishin* 38, 365–379.
- McGuire, J.J., 2008. Seismic cycles and earthquake predictability on East Pacific Rise transform faults. *Bull. Seismol. Soc. Am.* 98 (3), 1067–1084.
- McGuire, J.J., Collins, J.A., Gouédard, P., Roland, E., Lizarralde, D., Boettcher, M.S., Behn, M.D., Van Der Hilst, R.D., 2012. Variations in earthquake rupture properties along the Gofar transform fault, East Pacific Rise. *Nat. Geosci.* 5 (5), 336.
- McKenzie, D., Jackson, J., Priestley, K., 2005. Thermal structure of oceanic and continental lithosphere. *Earth Planet. Sci. Lett.* 233 (3), 337–349.
- Paige, C.C., Saunders, M.A., 1982. LSQR: sparse linear equations and least squares problems. *ACM Trans. Math. Softw.* 8 (2), 195–209.
- Peng, Z., Gomberg, J., 2010. An integrated perspective of the continuum between earthquakes and slow-slip phenomena. *Nat. Geosci.* 3 (9), 599–607.
- Pickle, R.C., Forsyth, D.W., Harmon, N., Nagle, A.N., Saal, A., 2009. Thermo-mechanical control of axial topography of intra-transform spreading centers. *Earth Planet. Sci. Lett.* 284 (3), 343–351.
- Roland, E., Lizarralde, D., McGuire, J.J., Collins, J.A., 2012. Seismic velocity constraints on the material properties that control earthquake behavior at the Quebrada-Discovery-Gofar transform faults, East Pacific Rise. *J. Geophys. Res., Solid Earth* 117 (B11). (1978–2012).
- Rubin, A.M., Gillard, D., Got, J.L., 1999. Streaks of microearthquakes along creeping faults. *Nature* 400 (6745), 635–641.
- Schaff, D.P., Bokelmann, G.H., Beroza, G.C., Waldhauser, F., Ellsworth, W.L., 2002. High-resolution image of Calaveras Fault seismicity. *J. Geophys. Res.* 107 (B9), 2186. <https://doi.org/10.1029/2001JB000633>.
- Segall, P., Rubin, A.M., Bradley, A.M., Rice, J.R., 2010. Dilatant strengthening as a mechanism for slow slip events. *J. Geophys. Res., Solid Earth* 115 (B12). (1978–2012).
- Segall, P., Bradley, A.M., 2012. The role of thermal pressurization and dilatancy in controlling the rate of fault slip. *J. Appl. Mech.* 79 (3), 031013.
- Takei, Y., 2002. Effect of pore geometry on V_p/V_s : from equilibrium geometry to crack. *J. Geophys. Res., Solid Earth* 107 (B2).
- Thurber, C.H., 1993. Local earthquake tomography: velocities and V_p/V_s theory. In: Iyer, H.M., Hirahara, K. (Eds.), *Seismic Tomography: Theory and Practise*. Chapman and Hall, New York, pp. 563–583.
- Waldhauser, F., Ellsworth, W.L., 2002. Fault structure and mechanics of the Hayward fault, California, from double-difference earthquake locations. *J. Geophys. Res.* 107 (B3). <https://doi.org/10.1029/2000JB000084>.
- Waldhauser, F., Ellsworth, W.L., Cole, A., 1999. Slip-parallel seismic lineations on the northern Hayward fault, California. *Geophys. Res. Lett.* 26 (23), 3525–3528.
- Waldhauser, F., Ellsworth, W.L., Schaff, D.P., Cole, A., 2004. Streaks, multiplets, and holes: high-resolution spatio-temporal behavior of Parkfield seismicity. *Geophys. Res. Lett.* 31 (18). <https://doi.org/10.1029/2004GL020649>.
- Yao, H., Gouédard, P., Collins, J.A., McGuire, J.J., van der Hilst, R.D., 2011. Structure of young East Pacific Rise lithosphere from ambient noise correlation analysis of fundamental- and higher-mode Scholte-Rayleigh waves. *C. R. Géosci.* 343 (8), 571–583.
- Zhang, H., Thurber, C.H., 2003. Double-difference tomography: the method and its application to the Hayward fault, California. *Bull. Seismol. Soc. Am.* 93 (5), 1875–1889.
- Zhang, H., Thurber, C., Bedrosian, P., 2009. Joint inversion for V_p , V_s , and V_p/V_s at SAFOD, Parkfield, California. *Geochem. Geophys. Geosyst.* 10 (11).
- Zhang, H., Thurber, C., Rowe, C., 2003. Automatic P-wave arrival detection and picking with multiscale wavelet analysis for single-component recordings. *Bull. Seismol. Soc. Am.* 93 (5), 1904–1912.
- Zhao, D., Hasegawa, A., 1993. P wave tomographic imaging of the crust and upper mantle beneath the Japan Islands. *J. Geophys. Res., Solid Earth* 98 (B3), 4333–4353.